Monthly Notices of the ROYAL ASTRONOMICAL SOCIETY

MNRAS **513,** 5766–5779 (2022) https://doi.org/10.1093/mnras/stac1282
Advance Access publication 2022 May 10

# Balancing turbulent heating with radiative cooling in blazars

Zachary Davis [1]★ Jesús M. Rueda-Becerril [2] and Dimitrios Giannios [1]

[1] *Department of Physics, Purdue University, 525 Northwestern Avenue, West Lafayette, IN 47907, USA*
[2] *Center for Computational Relativity and Gravitation, Rochester Institute of Technology, 85 Lomb Memorial Drive, Rochester, NY 14623, USA*

Accepted 2022 May 3. Received 2022 April 9; in original form 2022 January 21

## ABSTRACT

Recently, particle-in-cell (PIC) simulations have shown that relativistic turbulence in collisionless plasmas can result in an equilibrium particle distribution function where turbulent heating is balanced by radiative cooling of electrons. Strongly magnetized plasmas are characterized by higher energy peaks and broader particle distributions. In relativistically moving astrophysical jets, it is believed that the flow is launched Poynting flux dominated and that the resulting magnetic instabilities may create a turbulent environment inside the jet, i.e. the regime of relativistic turbulence. In this paper, we extend previous PIC simulation results to larger values of plasma magnetization by linearly extrapolating the diffusion and advection coefficients relevant for the turbulent plasmas under consideration. We use these results to build a single-zone turbulent jet model that is based on the global parameters of the blazar emission region, and consistently calculate the particle distribution and the resulting emission spectra. We then test our model by comparing its predictions with the broad-band quiescent emission spectra of a dozen blazars. Our results show good agreement with observations of low synchrotron peaked (LSP) sources and find that LSPs are moderately Poynting flux dominated with magnetization $1 \lesssim \sigma \lesssim 5$, have bulk Lorentz factor $\Gamma_j \sim 10$–$30$, and that the turbulent region is located at the edge, or just beyond the broad-line region (BLR). The turbulence is found to be driven at an area comparable to the jet cross-section.

**Key words:** acceleration of particles – radiation mechanisms: non-thermal – turbulence – BL Lacertae objects: general – quasars: general.

## 1 INTRODUCTION

In many astrophysical plasma flows, including those in supernova remnants, pulsar wind nebulae (PWNe), or active galactic nuclei (AGNs), a broad-band emission spectrum of electromagnetic radiation is often observed. AGNs, with a jet closely aligned to our line of sight, are referred to as blazars (Urry & Padovani 1995). Blazars have a characteristic double-peaked spectral energy distribution (SED). The first peak is attributed to synchrotron emission by ultrarelativistic electrons, and the second is likely to be the result of inverse Compton (IC) scattering off the same particles (Ghisellini et al. 1998). Blazars also exhibit intense flaring on short time-scales followed by quiescent intervals. Both the quiescent and flaring blazar SEDs are routinely explained by an extended, non-thermal, electron distribution that is usually modelled with a power law or broken power law (Ghisellini et al. 1998).

For the inferred non-thermal tails of the particle distribution to develop, an efficient particle acceleration mechanism needs to be in place, i.e. where the acceleration time-scale is shorter than, or of the order of, the variability time-scale in the emission region. The variability in the emission, especially for fast-evolving flares, puts strong constraints on the acceleration time-scales and the size of the emitting regions. There is an active debate on the particle acceleration mechanisms responsible for blazar flaring where shocks inside the jet flow (e.g. Spada et al. 2001; Böttcher & Dermer 2010; Mimica & Aloy 2012) or magnetic instabilities that result in magnetic reconnection in the jet (e.g. Giannios 2013) are commonly invoked. Regardless of the mechanism that powers the flaring events, at their non-linear stages, the dissipative mechanisms can be expected to drive turbulence within the jet flow (Baring, Böttcher & Summerlin 2016; Marscher 2016; Comisso & Sironi 2019). Turbulence in a strongly magnetized plasma (with magnetic energy density exceeding the plasma enthalpy density; also referred to as *relativistic turbulence*) has long been suspected to be an acceleration process for relativistic particles (Schlickeiser 1989). With recent magnetohydrodynamic (MHD) simulations suggesting that jets are launched as magnetically dominated plasma flows (Komissarov et al. 2007; Tchekhovskoy, McKinney & Narayan 2009; Barniol Duran, Tchekhovskoy & Giannios 2017), we may expect relativistic turbulence to drive part of the emission inside these outflows. In this work, we focus on a scenario where the more efficient particle acceleration processes operate at the onset of the jet instabilities and may power blazar flares while the resultant turbulence may be able to drive the quiescent and slow-evolving emission observed in blazars.

Our understanding of relativistic turbulence has substantially advanced recently thanks to particle-in-cell (PIC) simulations that explore particle acceleration in highly magnetized, turbulent plasmas (Comisso & Sironi 2018; Zhdankin et al. 2019). These simulations have shown that particles undergo an initial rapid acceleration phase from the current sheets created by the turbulence. After this, Alfvén

★ E-mail: zkd@purdue.edu

wave scattering, a second-order Fermi process (Fermi 1949), begins to dominate the acceleration and produces a non-thermal tail in the particle distribution (Comisso & Sironi 2018, 2019).

In the absence of substantial particle cooling, PIC simulations find that relativistic turbulence energizes particles to the system size-limited energy (Zhdankin et al. 2017). Inside the blazar emission region, however, we expect radiative losses to effectively cool the plasma resulting in a steady-state particle distribution as seen in Uzdensky (2018). The effects of radiative losses are particularly important to understand when studying the particle distribution in relativistic jets where radiative cooling time-scales are short. Currently, there are only a handful of PIC simulations that have studied relativistic turbulence that also include radiative cooling in the simulation (*radiative relativistic turbulence*). In particular, the results reported by Zhdankin et al. (2020) confirm the analytical results in Uzdensky (2018), concluding that steady states can be formed in a turbulent radiative plasma. In the same manner, Nättilä & Beloborodov (2021) show in their simulations that non-thermal tails develop in the particle distribution. Furthermore, the hard tail diffusion seems well described by Alfvén wave scattering theories (see Schlickeiser 1989). The previous works in relativistic turbulence mentioned above give key insights into the turbulent plasma properties inside of a blazar jet or similar environments. Though PIC simulations have greatly extended our understanding of relativistic plasmas, due to their computational cost, have only studied a small range of plasma magnetization and usually only include a few, if any, radiation mechanisms operating in jets.

In this work, we use the latest PIC findings for particle acceleration in relativistic turbulence, generalize the description of the acceleration terms for arbitrary magnetization $\sigma$, incorporate radiative cooling, and calculate the equilibrium particle distribution. We then proceed to build a simple single-zone model for the bulk properties of the turbulent region as expected in blazars and apply the model to a dozen sources with broad-band SED spectra. The target is twofold: (i) evaluate the feasibility of the model in accounting for the quiescent blazar SED; and (ii) extract important properties of the blazar zone such as bulk Lorentz factor, magnetization, and distance of the blazar zone from the central engine. This paper is organized as follows. Section 2 outlines our turbulent model. In Section 3, we describe the initial set-up and operation of the fitting algorithm used to test our model, as well as the best-fitting results. In Section 4, we further discuss our results in the context of blazar jet modelling. Finally, in Section 5, we present the conclusion from our findings.

## 2 EQUILIBRIUM PARTICLE DISTRIBUTION FROM TURBULENT ACCELERATION AND RADIATIVE COOLING

In this section, we build the model that describes the particle distribution of the fluid in the blazar emission region. The particle distribution is found as an equilibrium between the turbulent acceleration of particles and the radiative cooling mechanisms operating in these sources.

Turbulence is generated by large-scale fluctuations[1] that create a driving current at the boundary of the turbulent region, where energy cascades down to smaller scales via Alfvén waves with equivalent outgoing and incoming energy fluxes (see Goldreich & Sridhar 1995). The energy injected into the system through this process is a fraction of the stochastic magnetic energy that propagates the waves. Following Zhdankin et al. (2020), we will consider turbulence in the strong regime, where the fluctuations in magnetic field strength are comparable to the underlying background magnetic field, i.e. $\delta B_{\rm rms} \approx B_0$. The energy stored in the turbulent magnetic field will be dissipated into the particles over an Alfvén crossing time $\tau_{\rm a} \equiv R_{\rm T}/v_{\rm A}$, where $R_{\rm T}$ is the scale of the turbulence and $v_{\rm A} \equiv c\sqrt{\frac{\sigma}{\sigma+1}}$ is the Alfvén speed. Here, $\sigma = \frac{B_{\rm rms}^2}{4\pi h}$ is the plasma's magnetization or the plasma's ratio of magnetic energy to enthalpy $h$. With this, we parametrize the mean injected power as[2]

$$\langle \dot{E}_{\rm inj} \rangle = \eta_{\rm inj} \frac{B_0'^2}{8\pi n_0 \tau_{\rm a}}, \tag{1}$$

where $\eta_{\rm inj}$ is the fraction of turbulent magnetic energy deposited into the fluid and $n_0$ is the fluid's particle number density. The injected energy (equation 1) will heat the fluid until it escapes the turbulent area, or radiative losses balance the heating and create a steady state (Uzdensky 2018).

### 2.1 The particle acceleration model

The evolution of a particle energy distribution is described by the kinetic equation

$$\frac{\partial n(\gamma,t)}{\partial t} = \frac{1}{2}\frac{\partial^2}{\partial \gamma^2}\left[D(\gamma,t)n(\gamma,t)\right] + \frac{\partial}{\partial \gamma}\left[\dot{\gamma}(\gamma,t)n(\gamma,t)\right] + Q(\gamma,t) - \frac{n(\gamma,t)}{t_{\rm esc}}, \tag{2}$$

also known as the Fokker–Planck equation, where $Q(\gamma, t)$ is the particle injection rate, $D(\gamma, t)$ the particle diffusion coefficient, $n(\gamma, t)$ the differential particle distribution function, $\dot{\gamma}(\gamma, t)$ the energy-loss rate, $\gamma$ the particle Lorentz factor, $t$ the time variable, and $t_{\rm esc}$ is the particle escape time, i.e. the average time it takes for a particle to leave the system. This paper works under the assumption that the particle distribution starts and evolves isotropically. Though it should be noted that anisotropies in the particle distribution have been observed in PIC simulations (Comisso & Sironi 2019). We are interested in studying the steady-state particle distribution with negligible influence from particle injection or particle escape. Thus, we consider the case where $Q(\gamma, t) = 0$, and $t_{\rm esc} \to \infty$.

In this work, we are using the code PARAMO(Rueda-Becerril 2020) to solve the Fokker–Planck equation and calculate the emissivity. This code uses the Fokker–Planck in the same form as equation (2) and necessitates finding equivalent diffusion and cooling terms to the ones described in Zhdankin et al. (2020), which chooses to introduce the Fokker–Planck in the form

$$\frac{\partial n(\gamma,t)}{\partial t} = \frac{\partial}{\partial \gamma}\left(\gamma^2 D_{\rm pp}\frac{\partial}{\partial \gamma}\left(\frac{n(\gamma,t)}{\gamma^2}\right)\right) - \frac{\partial}{\partial \gamma}\left(A_{\rm p} n(\gamma,t) - \frac{\gamma^2}{\gamma_0 \tau_{\rm c}} n(\gamma,t)\right). \tag{3}$$

The last two expressions can be made equivalent by making the substitution

$$D(\gamma,t) = 2D_{\rm pp} \tag{4}$$

for the diffusion, and

$$\dot{\gamma} = -\left(A_{\rm p} + \frac{1}{\gamma^2}\partial_\gamma\left(\gamma^2 D_{\rm pp}\right) - \frac{\gamma^2}{\gamma_0 \tau_{\rm c}}\right) \tag{5}$$

[1] Defined as scales much larger than the scales of dissipation.

[2] Variables in the comoving frame of the plasma will be referenced with a prime symbol ($'$). Non-primed variables are assumed to be in the black hole rest frame unless explicitly stated.

for the energy-loss term. Where the term $\frac{\gamma^2}{\gamma_0 \tau_c}$ is the radiative cooling term discussed in Section 2.3, $\gamma_0$ is the mean Lorentz factor, and $\tau_c$ is the cooling time-scale.

Following the work done by Zhdankin et al. (2020), we model the diffusion coefficient quadratically in momentum and the advection coefficient linearly in momentum,

$$\begin{aligned} A_p &= (\Gamma_h \gamma_0 + \Gamma_a \gamma)/\tau_c, \\ D_{pp} &= \left(\Gamma_0 \gamma_0^2 + \Gamma_2 \gamma^2\right)/\tau_c. \end{aligned} \tag{6}$$

Here $\gamma_0$ represents the mean Lorentz factor of the particle distribution, $\tau_c$ represents the cooling time discussed in Section 2.3 and $\Gamma_i$ are constants that are contributing to the diffusion and advection coefficients discussed below.

The particle energy distribution is initialized set-up with a Maxwell–Jüttner distribution profile (Jüttner 1911),

$$f_0(\gamma) = \frac{\gamma^2 \beta}{\Theta K_2(1/\Theta)} \exp \frac{-\gamma}{\Theta}, \tag{7}$$

with $\Theta = K_B T / m_e c^2$, $K_B$ is the Boltzmann constant, and $\Theta$ is related to the mean Lorentz factor, in the ultrarelativistic limit, by $\Theta \approx \gamma_0/3$. Since we are working to a steady state, the initial injection temperature will have little effect on the final distribution (Zhdankin et al. 2020). Thus, the initial distribution is given a temperature very close to $\gamma_0/3$. We then allow the distribution to evolve for $t = \tau_c$ at which point the steady state has been reached.

To introduce the latest findings on turbulent particle acceleration from PIC simulations in our model, we use data from Zhdankin et al. (2020). The data contain the particle distribution for different values of magnetization ranging from $\sigma \sim 0.04$ to 12. For a given simulation, we time average the distribution after a steady state has been reached. The resultant time-averaged distributions are then fitted to the Fokker–Planck steady-state equation (8) (Zhdankin et al. 2020) using a Markov chain Monte Carlo (MCMC) method,

$$\begin{aligned} f_{ss}(\gamma) \approx k \left(\frac{\gamma}{\gamma_0}\right)^2 \left(1 + \left(\frac{\gamma}{\gamma_0}\right)^2\right)^{\Gamma_a/2\Gamma_2} \\ \times \exp\left(-\frac{\gamma}{\gamma_0 \Gamma_2} + \frac{\Gamma_h + 1}{\Gamma_2} \tan^{-1}\left(\frac{\gamma}{\gamma_0}\right)\right), \end{aligned} \tag{8}$$

where $k$ is a normalization constant. To maintain consistency with works like Comisso & Sironi (2019) and Wong et al. (2020), where the diffusion coefficient is expected to scale linearly with the magnetization $D_\gamma \sim 0.1\sigma \left(\frac{c}{l}\right) \gamma^2$ (here $l$ is the system size), we model the results for $\Gamma_i$ linearly with magnetization, arriving at[3]

$$\begin{aligned} \Gamma_0 &= \Gamma_2 = 0.05\sigma + 2.09, \\ \Gamma_a &= 0.124\sigma - 9.5, \\ \Gamma_h &= -0.42\sigma - 2.46. \end{aligned} \tag{9}$$

### 2.2 Blazar emission region

In this paper, the jet composition is an electron–ion plasma with relativistic electrons and cold ions that dominate the plasma's enthalpy. This results in a magnetization given by

$$\sigma = \frac{2u'_B}{n_p m_p c^2}, \tag{10}$$

where the ion particle density in the comoving frame $n_p$ is expected to be in equal partition with the electron particle density $n_e$ i.e. $n_e = n_p = n_0$.[4] In an electron–ion plasma, the energy partition between the two species of particles is still poorly understood. Previous works have shown that a significant portion of the turbulent energy is injected into the ions (Zhdankin et al. 2019). These results, however, are for low magnetization $\sigma < 1$. For $\sigma > 1$ we do not expect ions to necessarily have a dominant effect on the distribution since works like Howes (2010) predict a low ion to electron heating ratio for highly magnetized plasmas. In order to leave this effect for future works, we replace $\eta_{inj}$ with $\eta_{inj_e}$, where $\eta_{inj_e}$ specifically represents the amount of energy injected into the electron distribution. The magnetic field, as previously mentioned, is assumed to be strongly turbulent so that $B'^2_{rms} = B'^2_0 + \delta B'^2_{rms} = 2B'^2_0$ is true. Here $B'_0$ is related to the jet luminosity by

$$B'_0 = \sqrt{\frac{L_j 4\pi}{\Omega_j R_j^2 \Gamma_j^2 c}}, \tag{11}$$

where $\Omega_j = 2\pi(1 - \cos(1/\Gamma_j)) \approx \pi/\Gamma_j^2$ is the jet's solid angle (the approximation is not used in this paper), $L_j$ is the jets luminosity, $R_j$ is the distance from the black hole, $\Gamma_j$ is the jets bulk Lorentz factor, and we assume the jet opening angle is $1/\Gamma_j$. Further, the turbulent scale, $R_T$, is fraction of the jets cross-section,

$$R_T = R_{TM} \frac{R_j}{\Gamma_j}, \tag{12}$$

where $R_{TM}$ is the aforementioned fraction.

The particles accelerated by the jet are subject to radiation fields produced elsewhere in the blazar environment. Here, we assume the material is exposed to a radiation field from within the broad-line region (BLR). The BLR radiation field is assumed to be isotropic, monochromatic with frequency $\nu_0 = 10^{15}$ Hz and in the comoving frame, $\nu'_0 = \Gamma_j \nu_0$. We parametrize the BLR radiation in the lab frame using Ghisellini (2013),

$$u_{ph} = \frac{L_{BLR}}{4\pi c R_{BLR}^2}, \tag{13}$$

where $L_{BLR} \approx \eta_{ph} L_{disc}$ and $R_{BLR} \approx 10^{17} \sqrt{\frac{L_{disc}}{10^{45}}}$ cm (Ghisellini 2013). Further, our jet luminosity $L_j$ is modelled here to be directly proportional to the accretion power, i.e. $L_j = \eta_j \dot{M} c^2$. Similarly, we model the disc luminosity as directly proportional to the jet luminosity such that $L_{disc} = \frac{\eta_{disc}}{\eta_j} L_j$. For the coefficients $\eta_{disc}$ and $\eta_j$ we refer to Rueda-Becerril (2021) where $\eta_j \approx 1$ and $\eta_{disc} \approx 0.1$. Combining this information we get

$$u_{ph} \approx \eta_{ph}\, 0.26\, \mathrm{erg\,cm^{-3}}, \tag{14}$$

where $\eta_{ph}$ quantifies the amount of energy from the BLR photons that enter the emission region and $u'_{ph} = \Gamma_j^2(1 + \beta_j^2/3) u_{ph}$ is its value in the comoving frame (Dermer & Menon 2009). Here, $\beta_j$ is the jet's bulk velocity. This description suffices so long as the emission region is within the BLR. Outside of the BLR the photon density drops precipitously. To model this we follow Sikora et al. (2009), where inside the BLR we use the expression in equation (14). However, outside the BLR, the photon energy density drops with the cube of distance,

$$u_{ph} = \eta_{ph}\, 0.26\, \mathrm{erg\,cm^{-3}} \times \begin{cases} 1 & \text{for} \quad R_j \leqslant R_{BLR}, \\ \left(\frac{R_j}{R_{BLR}}\right)^{-3} & \text{for} \quad R_j > R_{BLR}, \end{cases} \tag{15}$$

[3] A comparison between the linear extrapolation done here and the PIC simulations done by Zhdankin 2020 can be seen in Fig.1.

[4] In this work, we focus on cold ion plasmas to maximize the magnetic energy per particle available at a given $\sigma$. Because of this, one can expect pair plasmas to require more extreme values of $\sigma$ to recreate similar results as seen in this paper.

with

$$R_{\rm BLR} = 10^{17}\sqrt{\frac{L_{\rm disc}}{10^{45}\,{\rm erg\,s^{-1}}}}\,{\rm cm} = 10^{17}\sqrt{\frac{\eta_{\rm disc}L_{\rm j}}{\eta_{\rm j}10^{45}\,{\rm erg\,s^{-1}}}}\,{\rm cm}. \quad (16)$$

### 2.3 Cooling and emission

So far, we have discussed how the particles are accelerated in the turbulent region. The particle acceleration is eventually balanced by radiative losses. Relativistic electrons in the blazar environment suffer from synchrotron and Compton losses. Here, we consider both the synchrotron self-Compton (SSC) and external inverse Compton (EIC) processes but limit our discussion to scattering in the Thomson limit (i.e. relativistic corrections to the electron scattering cross-section are ignored). For a relativistic plasma, the power lost per particle via synchrotron and EIC is (Rybicki & Lightman 1979)

$$\dot{\mathcal{E}}_{\rm syn} = \tfrac{4}{3}\sigma_{\rm T}cu'_{\rm B}\gamma^2, \quad (17a)$$

$$\dot{\mathcal{E}}_{\rm eic} = \tfrac{4}{3}\sigma_{\rm T}cu'_{\rm ph}\gamma^2, \quad (17b)$$

where $u'_{\rm B}$ is the magnetic energy density and is given by

$$u'_{\rm B} = \frac{B'^2_{\rm rms}}{8\pi} = \frac{B'^2_0 + \delta B'^2_{\rm rms}}{8\pi} = \frac{2B'^2_0}{8\pi}. \quad (18)$$

The plasma cooling is assumed to be dominated by synchrotron and EIC but the SSC component is added for completeness,

$$\dot{\mathcal{E}}_{\rm rad} = \dot{\mathcal{E}}_{\rm eic} + \dot{\mathcal{E}}_{\rm syn} + \dot{\mathcal{E}}_{\rm ssc}. \quad (19)$$

For the SSC cooling we follow Schlickeiser (2009) (derivation in Appendix A),

$$\dot{\mathcal{E}}_{\rm ssc} \approx \frac{3\pi\sigma_{\rm T}c_1q_0\epsilon_0^2R_{\rm T}}{2h^2}\gamma^2\int_0^\infty {\rm d}\gamma\,\gamma^2 n(\gamma,t) = \frac{3\pi\sigma_{\rm T}c_1q_0\epsilon_0^2R_{\rm T}n_0}{2h^2}\gamma^2\left\langle\gamma(t)^2\right\rangle. \quad (20)$$

The constant $c_1$ is found in Schlickeiser (1989),

$$c_1 = \int_0^\infty {\rm d}x\,xCS(x) = \frac{32}{81}\sqrt{3} = 0.684, \quad (21)$$

where $\epsilon_0$ and $q_0$ are given by

$$\epsilon_0 \approx \frac{he\,B'_{\rm rms}}{2\pi m_{\rm e}c}, \qquad q_0 = \frac{4\pi e^2}{\sqrt{3}c}, \quad (22)$$

and $h$ is the Planck constant. Since we are interested in the quiescent emission from a turbulent plasma that will reach a steady state, we assume that the SSC has maximum effect once the steady state is reached. With this assumption equation (20) becomes

$$\dot{\mathcal{E}}_{\rm ssc} \approx \frac{3\pi\sigma_{\rm T}c_1q_0\epsilon_0^2R_{\rm T}n_0}{2h^2}\gamma^2\left\langle\gamma(\tau_{\rm c})^2\right\rangle. \quad (23)$$

To find the equilibrium energy ($\gamma_0 m_{\rm e}c^2$), we balance the injected power with the radiated power,

$$\langle\dot{\mathcal{E}}_{\rm inj_e}\rangle = \langle\dot{\mathcal{E}}_{\rm rad}\rangle, \quad (24)$$

where $\langle\dot{\mathcal{E}}_{\rm rad}\rangle$ is the summation of all radiative losses:

$$\langle\dot{\mathcal{E}}_{\rm syn}\rangle = \frac{4}{3}\sigma_{\rm T}cu'_{\rm B}\left\langle\gamma^2\right\rangle,$$
$$\langle\dot{\mathcal{E}}_{\rm eic}\rangle = \frac{4}{3}\sigma_{\rm T}cu'_{\rm ph}\left\langle\gamma^2\right\rangle,$$
$$\langle\dot{\mathcal{E}}_{\rm ssc}\rangle \approx \frac{3\pi\sigma_{\rm T}c_1q_0\epsilon_0^2R_{\rm T}n_0}{2h^2}\left(\left\langle\gamma^2\right\rangle\right)^2. \quad (25)$$

Since the steady states formed in PIC simulation Zhdankin et al. (2020) can be approximated by a Maxwell–Jüttner distribution, we use the mean squared relation $\langle\gamma^2\rangle = \frac{4}{3}\langle\gamma\rangle^2 = \frac{4}{3}\gamma_0^2$. With this equation (25) becomes

$$\langle\dot{\mathcal{E}}_{\rm syn}\rangle = \frac{16}{9}\sigma_{\rm T}cu'_{\rm B}\gamma_0^2,$$
$$\langle\dot{\mathcal{E}}_{\rm eic}\rangle = \frac{16}{9}\sigma_{\rm T}cu'_{\rm ph}\gamma_0^2,$$
$$\langle\dot{\mathcal{E}}_{\rm ssc}\rangle \approx \frac{64\pi^2\sqrt{3}\sigma_{\rm T}c_1e^4R_{\rm T}n_0u'_{\rm B}}{m^2c^3}\gamma_0^4 = A_0R_{\rm T}n_0u'_{\rm B}\gamma_0^4. \quad (26)$$

Plugging equation (26) into equation (24) we get a quadratic for $\gamma_0^2$,

$$A_0R_{\rm T}n_0\gamma_0^4 + \frac{16}{9}\sigma_{\rm T}c\left(1+\frac{u'_{\rm ph}}{u'_{\rm B}}\right)\gamma_0^2 - \frac{\eta_{\rm inj_e}v_{\rm a}}{2n_0R_{\rm T}} = 0, \qquad a_1\gamma_0^4 + b_1\gamma_0^2 + c_2 = 0. \quad (27)$$

Solving for $\gamma_0$ leads to

$$\gamma_0 = \left(\frac{\left(b_1^2 - 4a_1c_2\right)^{\frac{1}{2}} - b_1}{2a_1}\right)^{\frac{1}{2}}. \quad (28)$$

Solving for $\frac{1}{\tau_{\rm c}} = \frac{\langle\dot{\gamma}\rangle}{\gamma_0}$,

$$\tau_{\rm c} = \left(\frac{16\sigma_{\rm T}c(u'_{\rm B}+u'_{\rm ph})}{9m_{\rm e}c^2}\gamma_0 + \frac{A_0n_0u'_{\rm B}R_{\rm T}}{m_{\rm e}c^2}\gamma_0^3\right)^{-1}, \quad (29)$$

where the $\tau_{\rm c}$ is the cooling time-scale of an electron with a Lorentz factor $\gamma_0$. Furthermore, $\langle\dot{\gamma}\rangle = \frac{\langle\dot{\mathcal{E}}_{\rm rad}\rangle}{m_{\rm e}c^2}$ and $\gamma_0$ is found using equation (28).

The last expressions for $\gamma_0$ and $\tau_{\rm c}$ are simplified when EIC or synchrotron are the dominant cooling processes. When SSC is negligible the cooling is dominated by EIC and synchrotron giving

$$\gamma_{0_{\rm nossc}} = \frac{3}{4}\left(\frac{\eta_{\rm inj_e}v_{\rm a}}{2n_0R_{\rm T}\sigma_{\rm T}c(1+u'_{\rm ph}/u'_{\rm B})}\right)^{\frac{1}{2}} \xrightarrow[\sigma\gg1]{} \frac{3}{4}\left(\frac{\eta_{\rm inj_e}}{2n_0R_{\rm T}\sigma_{\rm T}(1+u'_{\rm ph}/u'_{\rm B})}\right)^{\frac{1}{2}},$$
$$\tau_{\rm c_{nossc}} = \frac{9m_{\rm e}c^2}{16\sigma_{\rm T}c(u'_{\rm B}+u'_{\rm ph})\gamma_0}. \quad (30)$$

In the limit that either synchrotron or EIC is the sole dominant radiation mechanism,

$$\gamma_{0_{\rm i}} = \frac{3}{4}\left(\frac{\eta_{\rm inj_e}v_{\rm a}u'_{\rm B}}{2n_0R_{\rm T}\sigma_{\rm T}c(u_{\rm i})}\right)^{\frac{1}{2}} \xrightarrow[\sigma\gg1]{} \frac{3}{4}\left(\frac{\eta_{\rm inj_e}u'_{\rm B}}{2n_0R_{\rm T}\sigma_{\rm T}(u_{\rm i})}\right)^{\frac{1}{2}},$$
$$\tau_{\rm c_i} = \frac{9m_{\rm e}c^2}{16\sigma_{\rm T}c(u_{\rm i})\gamma_0}, \quad (31)$$

where $u_{\rm i}$ is $u'_{\rm ph}$ if EIC is dominant or $u'_{\rm B}$ if synchrotron is dominant. Using the synchrotron dominant case, the estimate for the synchrotron bolometric luminosity and synchrotron peak frequency are given below,

$$L_{\rm bol} \approx \eta_{\rm inj_e}L_{\rm j46}R_{\rm tm}^2\Gamma_{\rm j1}^2\,6.6\times10^{48}\,{\rm erg\,s^{-1}},$$
$$\nu_{\rm pk.syn} \approx \frac{\eta_{\rm inj_e}\sigma\Gamma_{\rm j1}^2}{R_{\rm tm}\sqrt{L_{\rm j46}}}\,3.6\times10^{12}\,{\rm Hz}. \quad (32)$$

Note that hereafter we adopt the notation $Q = Q_X\times10^X$ in CGS units.

The radiative cooling of the particle distribution results in an observable emission signature. Synchrotron luminosity from the emission region is calculated from the emissivity $j'_\nu$, under the assumption that radiation in the comoving frame is emitted isotropically (Gould 1979), while the emitting blob of plasma moves directly

**Table 1.** Initial fit parameter and ranges used in the fitting algorithm. Here $R_{\rm j} = R_{\rm j,18} \times 10^{18}$ cm and $L_{\rm j} = L_{\rm j,46} \times 10^{46}$ erg s$^{-1}$.

| Parameter | Initial | Min | Max |
|---|---|---|---|
| $\eta_{\rm inj_e}$ | 0.1 | 0.01 | 1 |
| $R_{\rm j,18}$ | 0.1 | $10^{-3}$ | $10^{2}$ |
| $R_{\rm TM}$ | 0.1 | $10^{-4}$ | 1 |
| $\eta_{\rm ph}$ | 0.1 | $10^{-4}$ | 1 |
| $L_{\rm j,46}$ | 1 | $10^{-3}$ | $10^{3}$ |
| $\Gamma_{\rm j}$ | 10 | 1 | 50 |
| $\sigma$ | 3 | 1 | 30 |

in line with the observer, i.e. the angle from the blobs motion to the line of sight of the observer $\theta_{\rm obs} = 0$,

$$\nu L_\nu = 3\frac{f(\tau'_{\nu'})}{\tau'_{\nu'}}\delta^4\left(\frac{4\pi}{3}\right)R_{\rm j}^3\nu' j'_{\nu'}, \tag{33}$$

where $\delta \equiv [\Gamma_{\rm j}(1-\beta\cos(\theta_{\rm obs}))]^{-1}$ is the Doppler factor, $\tau_\nu \equiv 2R_{\rm T}\kappa_\nu$, $\kappa_\nu$ is the synchrotron self-absorption coefficient, and

$$f(\tau) = \frac{1}{2} + \frac{\exp(-\tau)}{\tau} - \frac{1-\exp(-\tau)}{\tau^2} \tag{34}$$

is the optical depth function (Gould 1979). Compton luminosity is calculated similarly but since the only absorption mechanism we are incorporating is synchrotron self-absorption (SSA), Compton luminosity takes the form of

$$\nu L_\nu = \delta^4\left(\frac{4\pi}{3}\right)R_{\rm j}^3\nu' j'_{\nu' \rm c}, \tag{35}$$

where $j'_{\nu' \rm c}$ is the Compton emissivity.

### 2.4 Fitting algorithm

One of the main advantages of the model is the ability to test global parameters in a computationally efficient manner. To take full advantage of this, a fitting algorithm was developed in-house to compare the model predictions against other models or observations. This not only allows us to test the model by finding a good fit to data, but also to infer parameters about the physical systems.

The algorithm is a modified gradient descent algorithm. Instead of taking the gradient of the error each iteration, it instead takes the partial derivative of a given parameter for a set number of iterations before moving on to the next parameter,

$$g = \frac{\text{Error}[i] - \text{Error}[i-1]}{\text{Parameter}_j[i] - \text{Parameter}_j[i-1]}. \tag{36}$$

Here $g$ is the numerical partial derivative and $\text{Parameter}_j[i]$ denotes the value of a given parameter with index $j$ at the iteration $i$. For this work, $\text{Parameter}_j$ represents any one of the seven parameters found in Table 1. The Error$[i]$ is a user-defined error function that will compare the model to the 'true' data. For the work of this paper, we use a chi-squared function (Arfken, Weber & Harris 2013) to compare values from the 'true' data with values from the fit that have the closest $x$ coordinate. We then use this derivative to indicate the new parameter for the next iteration,

$$\text{Parameter}_j[i+1] = \text{Parameter}_j[i] - c_j g, \tag{37}$$

where $c_j$ is a constant multiple that slows down or speeds up the 'learning' process. It repeats this for a specified number of iteration and at the end shows the best fit. More details can be found at the GitHub page.[5]

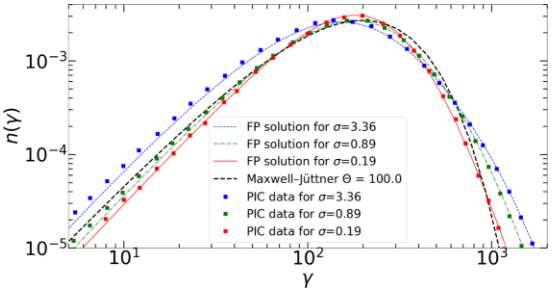


**Figure 1.** Comparison of the particle distribution found in the PIC simulations of Zhdankin et al. (2020) and our FP solver. The lines are FP solutions created using PARAMO (Rueda-Becerril 2020) with parameters to match the set-up in Zhdankin et al. (2020). The points depict the steady-state distribution found in Zhdankin et al. (2020, fig. 17). Red, green, and blue curves show the $\sigma = 0.19$, 0.89, and 3.36 cases, respectively. The black dashed curve is the Maxwell–Jüttner distribution for $\Theta = 100$.

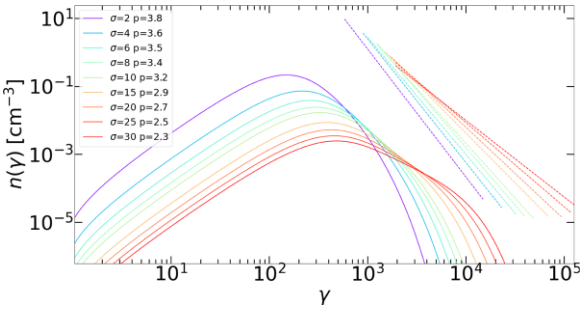


**Figure 2.** Steady-state particle distribution for varying $\sigma$ from 1 to 30 with $\eta_{\rm inj_e} = 1$, $R_{\rm m} = 1$, $R_{\rm j,18} = 0.4$, $L_{\rm j,46} = 1$, $\Gamma_{\rm j} = 1$, and $\eta_{\rm ph} = 0.1$. The colours indicate the value of $\sigma$ with solid lines representing the particle distribution and dashed lines are the power-law slope for the hardened part of the spectrum.

## 3 RESULTS

In this section, we explore the predictions of our model and how they compare with observations. First, we observe the effects of large values of magnetization ($\sigma > 10$) on the underlying particle distribution. Then we test our model's ability to reproduce a quiescent blazar SED. This is done by fitting our model to a dozen blazar SEDs found in Abdo et al. (2010).

### 3.1 Particle distribution

Turbulent acceleration is well modelled by resonant wave scattering or a second-order Fermi process (Schlickeiser 1989; Comisso & Sironi 2019; Demidem, Lemoine & Casse 2020; Zhdankin et al. 2020). With this comes the expectation for a hardened particle distribution above the thermal peak. The high-energy part of the distribution can be described by a power-law functional dependence with an index $p$. To analyse the particle distribution created by turbulent acceleration and its dependence on plasma magnetization, we computed several distributions by holding all model parameters constant except for $\sigma$, allowing it to vary in the range $1 \leq \sigma \leq 30$. This

[5] https://github.com/zkdavis/Base_ModelFitter.git

parametric study shows a hardening of the power-law spectra above the thermal peak for increasing magnetization.[6] Shown in Fig. 2, we note that this turbulent model predicts hard tails for large values of $\sigma$. However, the tails only span about an order of magnitude in particle energy. As discussed in Zhdankin et al. (2020), the steady-state distribution is mostly thermal at low $\sigma$ but changes to include a non-thermal tail as $\Gamma_a$ increases with $\sigma$. One can note from equation (8) that if $\Gamma_a$ and $\Gamma_h$ are negligible, as they are for low $\sigma$, we get back a Maxwell–Jüttner distribution. Furthermore, from equation (8), we can see the roles of the coefficients: $\Gamma_h$ determines the exponential cut-off and the fraction $\frac{\Gamma_a}{\Gamma_2}$ almost completely describes the power-law slope of the non-thermal particles. The particle power-law index is $p \propto 2 - \frac{\Gamma_a}{\Gamma_2}$. However, this dependence may break down for large $\sigma$ when $\Gamma_a > 0$ at which point it no longer describes an energy loss but rather a first-order Fermi-like energy gain.

### 3.2 Blazar fits

To test our model's ability to reproduce the quiescent emission of blazars, we use data from 12 sources from Abdo et al. (2010) that are representative populations of the total 48 quiescent SEDs reported in that work. The results of the blazar fits are best split into two categories. The first contains high synchrotron peaked (HSP) and intermediate synchrotron peaked (ISP) sources, while the second consists of the low synchrotron peaked (LSP) sources. Here LSP is defined as having a synchrotron peak frequency $\nu_{pk} \lesssim 10^{14}$ Hz, ISP has a peak synchrotron frequency of $10^{14} \lesssim \nu_{pk} \lesssim 10^{15}$ Hz, and HSP has $\nu_{pk} \gtrsim 10^{15}$ Hz (Abdo et al. 2010). All blazar SED and optical classifications are adopted from Abdo et al. (2010). Further, for discussion purposes, we will group ISP and HSP into one category referred to as HSP for all sources with $\nu_{pk} \gtrsim 10^{14}$ Hz.

To find the best fit for the seven free parameter used in our model, we apply the model fitter described in Section 2.4. This algorithm requires an initial guess and bounds for the parameters. The closer the initial guess, and the bounds around the guess, the less iterations are needed to get a fit. However, the bounds are usually left very large so as to account for any unique possibilities. All of which can be seen in Table 1. Parameters $\eta_{inj_e}$, $R_{TM}$, and $\eta_{ph}$ are all defined as a fraction of a whole so each of their maximum values are 1. The initial guess of 0.1 for each is based on the expectation that these will be a fraction and not an order of unity. The minimum of $10^{-4}$ for $\eta_{ph}$ is because we consider the case of negligible EIC cooling. The minimum of 0.01 for $\eta_{inj_e}$ is due to the fact that too little energy injected into the acceleration region would result in negligible emission. $R_{TM}$s range is large so that its dependence in this model can be studied. As can be seen in synchrotron limit (equation 32), $R_{TM}$ plays large role in dictating the peak frequency and bolometric luminosity. With the expectation that flaring events are caused by instabilities in the jet, and further that these instabilities later drive the turbulence, we expect the distance from the central engine to be related to the turbulence scales and thus related to the variability of the jet (Böttcher 2019),

$$R_j \approx \delta^2 c t_{v_{obs}} \Gamma_j R_{TM}^{-1} (1+z)^{-1}, \tag{38}$$

where $t_{v_{obs}}$ is the observed variation time, and $z$ is the redshift. For $\Gamma_j = 10, \theta_{obs} = 0, R_{TM} = 1, \Gamma_j = 1, z = 0$, and $t_{v_{obs}} = 1$ d from X-ray variability (Wagner & Witzel 1995), we get $R_j \approx 10^{17}$ cm. Thus, for an initial guess of $R_j$ we adopt similar values but left large bounds for model exploration. $\Gamma_j$ max constraints come from radio observations of $\Gamma_j \gtrsim 40$ being extremely rare (Lister 2016). Here, we limit our analysis to relativistic turbulence and so, adopt $\sigma \geq 1$. The initial guess of $\sigma = 3$ is comfortably in the relativistic plasma regime with the max of 30 to cover any extreme magnetization possibilities. $L_j$ range and initial guess is chosen to correspond with blazar luminosity range found in Ghisellini et al. (2017).

For each SED we fit the data from Abdo et al. (2010) by allowing the fitter to iterate 1000 times. At which point, they are rerun with the resultant best-fitting parameter as the initial values and the max and min bounds are shrunk around these new values. This process repeats until there is no noticeable reduction in error for a maximum of 4000 iterations. The best-fitting parameters are found in Tables 2 and 3 and the best-fitting SEDs can be found in Figs B1 and C1.

#### 3.2.1 *Low synchrotron peaked sources*

LSP sources make up seven out of the 12 sources used in this paper and include BL Lacertae objects (BL Lacs) and flat spectrum radio quasars (FSRQs). The resulting best-fitting SEDs for LSP sources can be seen in Fig. B1. These results are well described by our model. Generally, the fits exhibit a three-peaked structure with the SSC and EIC creating distinct peaks in what is generally the second peak in the typical double-peaked structure (Ghisellini et al. 2017). In Table 2, we can see that these sources exhibit a range of $\Gamma_j \sim 10$–$30$. A result that is consistent with most radio observations of LSP sources (Lister 2016). Magnetization for these fits operates in a modest range of $\sigma \approx$ 1–4.5. With $\sigma \approx 4$, according to Fig. 2, this would indicate a rather modest power-law index of about 3.6 for the underlying particle distribution. For the majority of LSP sources, we infer a turbulent region that is a fraction of the jet's cross-section with $R_{TM} \lesssim 0.5$, while the rest are close to 1. When comparing with Ghisellini et al. (2017), our LSP sources demonstrate a jet luminosity comparable to most blazars with $L_j$ between $10^{45}$ and $10^{46}$ erg s$^{-1}$.[7] The emission region for most of these sources is just outside of the BLR with the magnetic energy density staying comparable to BLRs photon field energy density (see Fig. 3). Still, all emission regions remain within a parsec from the central engine. The mean particle Lorentz factor range is $\gamma_0 \approx 100$–$200$.

#### 3.2.2 *High synchrotron peaked sources*

Contrary to the LSP fits, almost all of the HSP sources display double-peaked spectra (Fig. C1). Where the second peak is usually much broader and dominated by SSC emission. The model accurately describes the Compton peak but does not seem to be able to create as broad a synchrotron peak. HSP best-fitting parameters are much more extreme than that of the LSP.[8] This is perhaps best shown in Fig. 4, where one notices a large jump in baryon number $\mu$ separating the HSP sources from the LSP sources. Here, we define the jet baryon number as $\mu = \Gamma_j(1+\sigma)$, which also corresponds to the asymptotic bulk Lorentz factor of the jet provided that all the magnetic energy

[6] The power laws are computed by averaging the slope from the peak to two standard deviations past the peak Lorentz factor, i.e. it is averaged from $\gamma_{pk}$ to a Lorentz factor $\gamma_2$, where $\gamma_2$ satisfies the condition: $n(\gamma_2 > \gamma_{pk}) = n(\gamma_{pk}) -$ standard deviation$(n(\gamma))*2$.

[7] An exception is made here for J1719.3+1746. Though it is an LSP according to Abdo et al. (2010), our fits would better describe this as an HSP source.

[8] It should be noted that of this group, J2000.2+6506 is a clear outlier in our results. Though Abdo et al. (2010) initially categorized this as an HSP our fit is that of an LSP and thus the resulting fit being much closer to that of LSP sources is due to phenomenological fitting.

**Table 2.** Best-fitting parameters found after a maximum of 4000 iterations.

| Object | SED type | Optical type | $\eta_{\mathrm{inj_e}}$ | $R_{\mathrm{j},18}$ | $R_{\mathrm{TM}}$ | $\eta_{\mathrm{ph}}$ | $L_{\mathrm{j},46}$ | $\Gamma$ | $\sigma$ |
|---|---|---|---|---|---|---|---|---|---|
| J0238.4+2855 | LSP | FSRQ | 0.65 | 0.341 | 0.434 | 0.964 | 1 | 14.09 | 2.08 |
| J0137.1+4751 | LSP | FSRQ | 0.767 | 0.288 | 1 | 0.581 | 0.317 | 10.67 | 4.15 |
| J1159.2+2912 | LSP | FSRQ | 0.885 | 0.105 | 0.684 | 0.436 | 0.145 | 13.61 | 1.56 |
| J1256.1−0547 | LSP | FSRQ | 0.212 | 0.998 | 0.3 | 0.612 | 3.295 | 17.57 | 3.82 |
| J0238.6+1636 | LSP | BL Lac | 0.307 | 2.609 | 0.886 | 0.991 | 1.584 | 21.62 | 1.23 |
| J0855.4+2009 | LSP | BL Lac | 0.201 | 0.412 | 1 | 0.162 | 0.245 | 12.7 | 4.56 |
| J1719.3+1746 | LSP | BL Lac | 0.989 | 3.111 | 1.97E-03 | 0.731 | 127.544 | 30.39 | 1.07 |
| J1058.9+5629 | ISP | BL Lac | 0.425 | 1.06E-03 | 0.481 | 0.179 | 7.98E-03 | 23.29 | 8.47 |
| J1221.7+2814 | ISP | BL Lac | 0.323 | 0.047 | 9.51E-03 | 0.781 | 14.571 | 36.61 | 3.33 |
| J0449.7−4348 | HSP | BL Lac | 0.284 | 0.018 | 0.124 | 0.198 | 1 | 21.92 | 14.38 |
| J2000.2+6506 | HSP | BL Lac | 0.051 | 10.563 | 0.274 | 0.076 | 3.194 | 13.01 | 4.98 |
| J2158.8−3014 | HSP | BL Lac | 0.082 | 9.67E-03 | 0.049 | 0.992 | 7.087 | 46.06 | 14.02 |

**Table 3.** Best-fitting results found after a maximum of 4000 iterations. All values are in CGS units.

| Object | SED type | Optical type | $L_{\mathrm{J}}$ | $R_{\mathrm{j}}$ | $R_{\mathrm{T}}$ | $\gamma_0$ | $u_{\mathrm{B}}$ | $u_{\mathrm{ph}}$ | $n_0$ |
|---|---|---|---|---|---|---|---|---|---|
| J0238.4+2855 | LSP | FSRQ | 1.00E + 46 | 3.41E + 17 | 1.05E + 16 | 112.11 | 0.915 | 1.708 | 585.46 |
| J0137.1+4751 | LSP | FSRQ | 3.17E + 45 | 2.88E + 17 | 2.70E + 16 | 230.69 | 0.407 | 0.175 | 130.53 |
| J1159.2+2912 | LSP | FSRQ | 1.45E + 45 | 1.05E + 17 | 5.27E + 15 | 149.68 | 1.403 | 1.370 | 1.19E + 03 |
| J1256.1−0547 | LSP | FSRQ | 3.30E + 46 | 9.98E + 17 | 1.70E + 16 | 132.81 | 0.351 | 0.402 | 122.43 |
| J0238.6+1636 | LSP | BL Lac | 1.58E + 46 | 2.61E + 18 | 1.07E + 17 | 137.93 | 0.025 | 0.018 | 26.67 |
| J0855.4+2009 | LSP | BL Lac | 2.45E + 45 | 4.12E + 17 | 3.25E + 16 | 215.07 | 0.153 | 0.016 | 44.66 |
| J1719.3+1746 | LSP | BL Lac | 1.28E + 48 | 3.11E + 18 | 2.01E + 14 | 305.9 | 1.399 | 11.419 | 1.74E + 03 |
| J1058.9+5629 | ISP | BL Lac | 7.98E + 43 | 1.06E + 15 | 2.19E + 13 | 239.26 | 755.002 | 34.282 | 1.19E + 05 |
| J1221.7+2814 | ISP | BL Lac | 1.46E + 47 | 4.72E + 16 | 1.23E + 13 | 149.01 | 694.979 | 370.475 | 2.78E + 05 |
| J0449.7−4348 | HSP | BL Lac | 1.00E + 46 | 1.79E + 16 | 1.01E + 14 | 179.44 | 330.33 | 33.642 | 3.06E + 04 |
| J2000.2+6506 | HSP | BL Lac | 3.19E + 46 | 1.06E + 19 | 2.23E + 17 | 327.78 | 0.003 | 2.19E-5 | 0.81 |
| J2158.8−3014 | HSP | BL Lac | 7.09E + 46 | 9.67E + 15 | 1.04E + 13 | 61.7 | 8.04E + 03 | 744.511 | 7.63E + 05 |

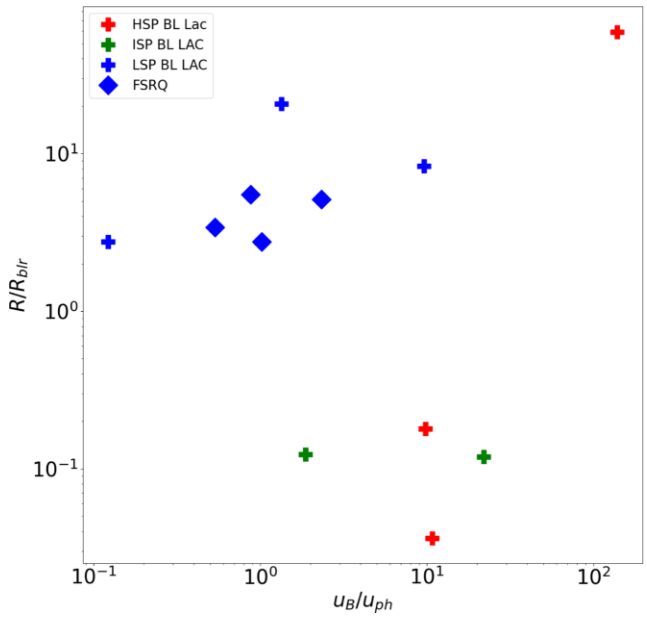


**Figure 3.** The *y*-axis displays how far a given source is from the central engine compared with the edge of the BLR region. In the *x*-axis we compare magnetic energy density to the BLR photon energy density.

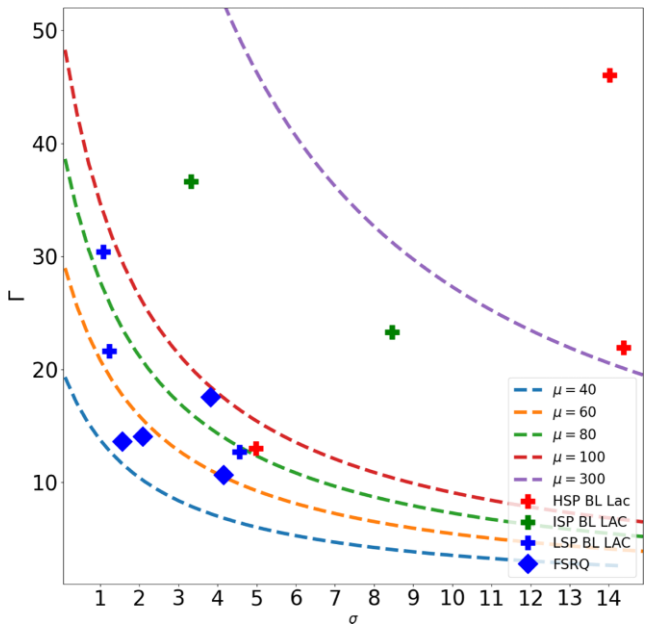


**Figure 4.** We plot a given source's bulk Lorentz factor versus its magnetization. The dashed lines are baryon loading contours for values $\mu = 40$, 60, 80, 100, and 300.

was to be converted into bulk motion. From the same Fig. 4, we can see $\Gamma_{\mathrm{j}}$ ranges from 10 to 50. The large $\Gamma_{\mathrm{j}}$ was not expected since the sources are all BL Lac objects and do not typically exhibit large Lorentz boosted Compton peak like that of FSRQs (Ghisellini et al. 2017). As one might expect to have more energetic particles to account for the higher energy of emission in HSPs, the magnetization for these sources is much higher than the LSP sources, with $\sigma_{\mathrm{ave}} \approx 9$. This would also explain the higher magnetic energy density to

photon field energy density seen in these sources in Fig. 3. The jet luminosity of these sources varies from $10^{44}$ to $10^{47}$ erg s$^{-1}$. Emission regions for these sources are much closer to the central engine with $R_{\rm j} \approx 10^{15}$–$10^{16}$ cm. Following this, we infer more compact turbulent region and $R_{\rm TM}$ about 10 times smaller than that of the LSPs. Particle number density for the sources also seems to be much larger than the LSP sources with some having $n_0 \approx 10^5$ cm$^{-3}$. This is probably needed to create the large SSC emission that dominates these SEDs. With them being much closer to the central engine, these sources all have the emission region well within the BLR (see Fig. 3).

## 4 DISCUSSION

Our model of turbulent acceleration has a unique advantage in that the particle distribution is not picked by hand but, rather, arises from the physical properties of the large-scale emission region. Typically, modelling of the particle distribution inside relativistic jets is done by assuming the particles form a power law with an index $p$ within a range $\gamma_{\rm min}$ through $\gamma_{\rm max}$, or by more complicated particle distributions. Quantities such as $p$, $\gamma_{\rm min}$, and $\gamma_{\rm max}$ are usually treated as free parameters. This non-thermal particle distribution is then injected into a region where it cools radiatively while slowly escaping the emission region. In works such as Böttcher et al. (2013), a steady state can be reached by balancing the injection of non-thermal particles with radiative cooling and particle escape. Fits from Böttcher et al. (2013) are able to constrain the Doppler factor and can be compared to ours. For the source J12561.1−0547 (3C 279), Böttcher et al. (2013) find $\delta = 17$. Though $\delta$ is highly dependent on the observer angle, for our assumption of $\theta_{\rm obs} = 0$ we found a $\delta \approx 35$. Putting our result within the bounds of superluminal studies such as Bloom, Fromm & Ros (2013) where the, admittedly broad, range is $\delta \approx 20$–$80$.

This work considers a scenario where turbulence is generated at the non-linear stages of instabilities within the jet. The resulting turbulence energizes electrons that, at the same time, experience radiative losses. As a result of a balance of energization and cooling, the particles in the turbulent plasma acquire a steady-state distribution that has a distinctly non-thermal appearance. The emission of the electrons may be of relevance to the observed blazar emission, and in particular to the quiescent emission seen in these sources. As can be seen in Fig. 2, the heating/cooling balance in the turbulent region results in a narrow particle distribution for modest particle magnetization $\sigma \sim 1$. While, for sufficient high magnetization, the distribution broadens. In the case of high magnetization, we find extended particle distribution that can be approximated by a power law for about an order of magnitude in energy above the peak of the distribution. We can see in the SEDs found in Figs B1 and C1 that this translates into smooth emission spectra that describe the quiescent emission observed in blazars well. Aside from the quiescent emission, of focus in this work, this model may have implications for blazar variability. In Marscher (2014) turbulent plasma is used to account for observations of rapid variability in radiative flux and polarization seen in multiwavelength blazar observations by simulating turbulence with a large set of plasma cells that have a randomly oriented, but otherwise smooth, magnetic field. The collective emission from these cells should be similar to the turbulent region model described here.

The best-fitting values for the jet magnetization and bulk Lorentz factor inferred from the model show consistency with the model put forward in Rueda-Becerril, Harrison & Giannios (2021), where the majority of the sources appear to be launched with a similar baryon loading parameter $\mu \approx 40$–$100$. In Fig. 4, this is shown with the noted exception of the HSP sources. HSPs appear to require significantly larger magnetization $\mu \approx 350$ from other blazar sources. Although the model does not fit the spectrum of the HSP sources well, there may still be some information to glean from the comparison. We find that the model generally favours a dense emission region for HSPs that is close to the central engine. We can gather an understanding of how the fits reach different peaks in luminosity and frequency by looking at the synchrotron limit equation (32). In order to get to these high synchrotron frequencies, the turbulent scale needs to drop. However, the smaller the emission region, the dimmer the source. Though most of the HSP sources tend to be dimmer, the squared dependence of the luminosity with $R_{\rm TM}$ is a steep one. The fitted model parameters may turn out to be less extreme if one includes Klein–Nishina (KN) correction to Compton scattering, neglected in this study. The HSP sources are dominated by SSC cooling and the reduction of the SSC cooling efficiency because of relativistic corrections would allow the particles to reach a higher $\gamma_0$ and broaden the synchrotron emission for the same parameters. The KN corrections will tend to result in smaller values for $\mu$ for HSP sources, since the drop in cooling efficiency provided by the KN cross-section may drop the energy per baryon required to reach such high synchrotron peaks. It may also be the case that the extreme fit parameters simply suggest that HSP sources require more efficient acceleration than the turbulence prescription adopted here.

### 4.1 Future extensions to the model

Currently, few PIC simulations have studied relativistic turbulence. This work is based on the PIC simulations in Zhdankin et al. (2020) in which only a handful of simulations, which cover a small range of plasma magnetization, are reported. One could use Alfvén wave scattering to describe the diffusion in the plasma. Simulations have shown this to be a consistent description (Comisso & Sironi 2019) but without an analytic model for the advection coefficient, our only means to improve our diffusive model is to include more PIC simulation data at additional magnetizations.

In this model, we focused on a plasma whose internal energy is dominated by cold ions. Further, we use the free parameter $\eta_{\rm inj_e}$ to parametrize the energy injected into the electrons from the turbulent cascade. There is not much to suggest that this should be constant. In Zhdankin et al. (2019) the authors find that the energy in the non-thermal electrons gain scales with $E_{\rm nt} \propto (\rho_{\rm e}/\rho_{\rm i})^{2/3}$, where $\rho_{\rm e}$ and $\rho_{\rm i}$ are the electron and ion gyroradii, respectively. However, this result is from a PIC simulation whose plasma magnetization is less unity contrary to the focus of our work. Estimates for the ion to electron heating ratio (Howes 2010) do show an expectation for marginal ion heating for high plasma magnetization. Regardless to simulate a larger range of plasma composition, magnetizations, and energies, future works will need to model the ion heating and that of the electrons.

In this work, we develop a simple single-zone model for the blazar region but extending this model to include multiple emission zones should be straightforward. The easiest approach might be one similar to that found in Boula, Mastichiadis & Kazanas (2021) where the cooling and heating take place in distinct regions. One can imagine having the steady state reached before exiting an acceleration region. The acceleration region could have minimum external photon cooling and create a steady state by balancing turbulent heating with the synchrotron losses alone. Once exiting the acceleration region, the particles would then be exposed to photon fields like those of the BLR. This would effectively separate the parameters of the jet that create the synchrotron peak from those that create the Compton

peak. This two-zone model would still use a particle distribution that arises from the global parameters of the emission region, reducing the assumption about the particle acceleration, but would also allow us to compute the synchrotron and Compton emission with model parameters that are independent of each other.

Another natural extension to this model is to account for the time-dependent nature of blazar emission. For instance, one may recreate and build on a scenario similar to the minijet model proposed in Giannios, Uzdensky & Begelman (2009). Here, instead of a single turbulent region to represent the total acceleration region, one can envision several compact turbulent regions each resulting in non-thermal particle acceleration that contributes to the total emission. This picture may be particularly applicable to HSP sources with the smaller inferred values $R_{\rm TM}$ possibly representing compact turbulent regions within the jet. Such regions may be driven by plasma outflowing from large-scale reconnecting current sheets. The fast-evolving flares originate in the current sheets (Christie et al. 2019), while slower evolving and quiescent emission is the result of the turbulent heating discussed here.

## 5 CONCLUSION

In this paper, we have constructed a turbulent jet model that incorporates the plasma physics from PIC simulations while being computationally efficient enough to constrain the physical properties of blazars. By analysing work done by Zhdankin et al. (2020), we found diffusion and advection coefficients that can describe a particle distribution at much larger scales and magnetizations than PIC simulations have available while retaining the crucial microscopic physics from the simulations. We then used this information to build a single-zone turbulent jet model where the emission comes from a blob of plasma in which particles are accelerated by turbulence and cooled radiatively. Since turbulence may not be a fast enough accelerator to account for, say, fast-evolving, intense flaring blazar events, we focused on the model's ability to recreate the observed quiescent emission. Using data from Abdo et al. (2010), we compared our model predictions against the broad-band SEDs of 12 blazars. We did this by performing a fit of the seven free parameters in the model over a large parameter domain. These seven parameters are key insights into the blazar's emission region. For LSP sources we found that the emission region is typically at the, or slightly beyond, edge of the BLR region. The emission region's size itself is typically a modest fraction of a cross-section of the jet but could be an order of unity. Perhaps hinting at distinct instabilities that trigger turbulence in different sources. The magnetization inferred by the model suggests that LSP sources are moderately Poynting dominated with $\sigma = 1$–$5$ with a bulk Lorentz factor in the range of 10–30. Contrary to the LSP sources, the HSP and ISP sources are generally less satisfactory fits that require more extreme parameters. HSPs and ISPs require dense emission regions that are closer to the central engine. These jets are inferred to be largely Poynting flux dominated with $\sigma = 5$–$15$ and have extreme bulk Lorentz factors up to 50. While the HSP and ISP fits are extreme, our model accurately reproduces quiescent emission from LSP blazars. It is able to do this with a successful turbulent model that accurately encodes expensive results from PIC simulations into a computationally efficient kinetic description of the turbulent plasma.

## ACKNOWLEDGEMENTS

We would like to thank Vladimir Zhdankin for providing additional PIC results that helped to improve our physical modelling, and for his insightful comments. We are very grateful for the insightful comments offered by Maria Petropoulou and an anonymous referee. ZD and DG acknowledge support from the Fermi Cycle 14 Guest Investigator Program 80NSSC21K1951, 80NSSC21K1938, and the NSF AST-2107806 grants. JMR-B acknowledges support from the NSF AST-2009330 grant.

Additional software used: MATPLOTLIB (Hunter 2007) and NUMPY (Harris et al. 2020).

## DATA AVAILABILITY

Particle distributions and emissions were calculated using the code PARAMO (Rueda-Becerril 2020). Additional PIC results from the paper Zhdankin et al. (2020) were acquired through private correspondence. Source data used to fit the SEDs in Figs B1 and C1 were taken from Abdo et al. (2010). WEBPLOTDIGITIZER was used for extraction. The fitting algorithm used to get the final fits was developed in-house and can be found at: https://github.com/zkdavis/Base_ModelFitter.git. Results from the fits are available in the paper and its supplementary material.

## REFERENCES

Abdo A. A. et al., 2010, ApJ, 716, 30
Arfken G., Weber H., Harris F., 2013, Mathematical Methods for Physicists: A Comprehensive Guide. Elsevier Science, Amsterdam
Baring M. G., Böttcher M., Summerlin E. J., 2016, MNRAS, 464, 4875
Barniol Duran R., Tchekhovskoy A., Giannios D., 2017, MNRAS, 469, 4957
Bloom S. D., Fromm C. M., Ros E., 2013, AJ, 145, 12
Böttcher M., 2019, Galaxies, 7, 20
Böttcher M., Dermer C. D., 2010, ApJ, 711, 445
Böttcher M., Reimer A., Sweeney K., Prakash A., 2013, ApJ, 768, 54
Boula S., Mastichiadis A., Kazanas D., 2021, PoS, ICRC2021, 678
Christie I. M., Petropoulou M., Sironi L., Giannios D., 2019, MNRAS, 482, 65
Comisso L., Sironi L., 2018, Phys. Rev. Lett., 121, 255101
Comisso L., Sironi L., 2019, ApJ, 886, 122
Crusius A., Schlickeiser R., 1986, A&A, 164, L16
Crusius A., Schlickeiser R., 1988, A&A, 196, 327
Demidem C., Lemoine M., Casse F., 2020, Phys. Rev. D, 102, 023003
Dermer C. D., Menon G., 2009, High Energy Radiation from Black Holes: Gamma Rays, Cosmic Rays, and Neutrinos. Princeton Univ. Press, Princeton, NJ
Fermi E., 1949, Phys. Rev., 75, 1169
Ghisellini G., 2013, Lecture Notes in Physics Vol. 873, Radiative Processes in High Energy Astrophysics. Springer, Cham, Switzerland
Ghisellini G., Celotti A., Fossati G., Maraschi L., Comastri A., 1998, MNRAS, 301, 451
Ghisellini G., Righi C., Costamante L., Tavecchio F., 2017, MNRAS, 469, 255
Giannios D., 2013, MNRAS, 431, 355
Giannios D., Uzdensky D. A., Begelman M. C., 2009, MNRAS, 395, L29
Goldreich P., Sridhar S., 1995, ApJ, 438, 763
Gould R., 1979, A&A, 76, 306
Harris C. R. et al., 2020, Nature, 585, 357
Howes G. G., 2010, MNRAS, 409, L104
Hunter J. D., 2007, Comput. Sci. Eng., 9, 90
Jüttner F., 1911, Ann. Phys., 339, 856
Komissarov S. S., Barkov M. V., Vlahakis N., Königl A., 2007, MNRAS, 380, 51
Lister M., 2016, Galaxies, 4, 29
Marscher A. P., 2014, ApJ, 780, 87
Marscher A., 2016, Galaxies, 4, 37
Mimica P., Aloy M. A., 2012, MNRAS, 421, 2635
Nättilä J., Beloborodov A. M., 2021, ApJ, 921, 87

Rueda-Becerril J. M., 2020, Astrophysics Source Code Library, record ascl:2009.008
Rueda-Becerril J. M., 2021, Astron. Nachr., 342, 277
Rueda-Becerril J. M., Harrison A. O., Giannios D., 2021, MNRAS, 501, 4092
Rybicki G. B., Lightman A. P., 1979, Radiative Processes in Astrophysics. Wiley, New York
Schlickeiser R., 1989, ApJ, 336, 243
Schlickeiser R., 2009, MNRAS, 398, 1483
Sikora M., Stawarz Ł., Moderski R., Nalewajko K., Madejski G. M., 2009, ApJ, 704, 38
Spada M., Ghisellini G., Lazzati D., Celotti A., 2001, MNRAS, 325, 1559
Tchekhovskoy A., McKinney J. C., Narayan R., 2009, ApJ, 699, 1789
Urry C. M., Padovani P., 1995, PASP, 107, 803
Uzdensky D. A., 2018, MNRAS, 477, 2849
Wagner S. J., Witzel A., 1995, ARA&A, 33, 163
Wong K., Zhdankin V., Uzdensky D. A., Werner G. R., Begelman M. C., 2020, ApJ, 893, L7
Zhdankin V., Werner G. R., Uzdensky D. A., Begelman M. C., 2017, Phys. Rev. Lett., 118, 055103
Zhdankin V., Uzdensky D. A., Werner G. R., Begelman M. C., 2019, Phys. Rev. Lett., 122, 055101
Zhdankin V., Uzdensky D. A., Werner G. R., Begelman M. C., 2020, MNRAS, 493, 603

## SUPPORTING INFORMATION

Supplementary data are available at *MNRAS* online.

**all_params.csv**

Please note: Oxford University Press is not responsible for the content or functionality of any supporting materials supplied by the authors. Any queries (other than missing material) should be directed to the corresponding author for the article.

## APPENDIX A: STEADY-STATE SSC COOLING IN STOCHASTIC MAGNETIC FIELDS

Starting with power radiated via synchrotron (Rybicki & Lightman 1979, equation 6.33):

$$p_{\rm s}(\nu) = \frac{\sqrt{3}e^3 B \sin\theta \nu}{mc^2 \nu_{\rm c}} F\left(\frac{\nu}{\nu_{\rm c}}\right) \ {\rm erg\,s^{-1}\,Hz^{-1}}, \tag{A1}$$

$$\nu_{\rm c} = \frac{3\gamma^2 eB\sin\theta}{4\pi mc} = \frac{3}{2}\nu_0\gamma^2. \tag{A2}$$

Here, $\theta$ is the pitch angle of the particle, $\gamma$ is the particles Lorentz factor, and $F$ is

$$F(x) = \int_{\frac{x}{\sin\theta}}^{\infty} K_{5/3}(z)\,{\rm d}z. \tag{A3}$$

Combining (A1) and (A2) we get

$$p_{\rm s} = \frac{4\pi e^2 \nu}{\sqrt{3}c\gamma^2} F\left(\frac{\nu}{\nu_{\rm c}}\right) \ {\rm erg\,s^{-1}\,Hz^{-1}}. \tag{A4}$$

In a turbulent media the synchrotron power needs to be averaged over scattering angles. Here we follow Crusius & Schlickeiser (1988),

$$p_{\rm rs} = \frac{q_0\nu}{\gamma^2}\int_0^{2\pi}{\rm d}\phi\int_0^{\pi}{\rm d}\theta\ \sin\theta\int_{\frac{x}{\sin\theta}}^{\infty}{\rm d}z\ K_{5/3}(z)\,{\rm erg\,s^{-1}\,Hz^{-1}}. \tag{A5}$$

In Crusius & Schlickeiser (1986) it was shown that

$$\int_0^{\pi}{\rm d}\theta\ \sin\theta\int_{\frac{x}{\sin\theta}}^{\infty}{\rm d}z\ K_{5/3}(z) = \pi\,{\rm CS}(x), \tag{A6}$$

where

$${\rm CS}(x) = W_{0,\frac{4}{3}}(x)W_{0,\frac{1}{3}}(x) - W_{\frac{1}{2},\frac{5}{6}}(x)W_{\frac{-1}{2},\frac{5}{6}}(x), \tag{A7}$$

and $W_{i,j}$ denotes the Whittaker's function. Giving us an expression for the emitted power via synchrotron in a stochastic magnetic field (A8),

$$p_{\rm rs}(\nu) = \frac{q_0\nu}{\gamma^2}\frac{\pi}{2}{\rm CS}\left(\frac{\nu}{\nu_{\rm c}}\right) \ {\rm erg\,s^{-1}\,Hz^{-1}}. \tag{A8}$$

It is easier to keep up with Schlickeiser's derivation (Schlickeiser 2009) if we switch power from frequency dependence to energy dependence:

$$p(\nu) = \frac{{\rm d}\epsilon}{{\rm d}\nu\,{\rm d}t}\,{\rm erg\,s^{-1}\,Hz^{-1}} \rightarrow p(\epsilon) = \frac{{\rm d}\epsilon}{{\rm d}\epsilon\,{\rm d}t} = \frac{1}{h}p\left(\nu = \frac{\epsilon}{h}\right)\,{\rm s^{-1}}. \tag{A9}$$

This turns equation (A8) into

$$p_{\rm rs}(\epsilon) = \frac{q_0\epsilon}{\gamma^2 h^2}\frac{\pi}{2}{\rm CS}\left(\frac{\epsilon}{\epsilon_{\rm c}}\right)\ {\rm s^{-1}}. \tag{A10}$$

Now let us take a look at what the power emitted via SSC should be (Schlickeiser 2009, equation 4.2),

$$p_{\rm ssc}(\epsilon_\gamma,\gamma) = c\epsilon_\gamma\int_0^{\infty}{\rm d}\epsilon\, n_{\rm s}(\epsilon)\sigma(\epsilon_\gamma,\epsilon,\gamma)\,{\rm s^{-1}}. \tag{A11}$$

The total power can be found by integrating over the scattered energies,

$$P_{\rm ssc}(\epsilon_\gamma, \gamma) = c \int_0^\infty {\rm d}\epsilon_\gamma\, \epsilon_\gamma \int_0^\infty {\rm d}\epsilon\, n_{\rm s}(\epsilon)\sigma(\epsilon_\gamma, \epsilon, \gamma)\,{\rm erg\,s^{-1}}. \tag{A12}$$

Here, $n_{\rm s}$ is the number density of scattered photons, $\epsilon_\gamma$ is the scattered photon energy, $\gamma$ is the electron's Lorentz factor, $\sigma$ is the interaction cross-section, and $\epsilon$ is the photons pre-scattered energy. The cross-section is given by Schlickeiser (2009, equation 4.2.1):

$$\sigma(\epsilon_\gamma, \epsilon, \gamma) = \frac{3\sigma_{\rm T}}{4\epsilon\gamma^2} G(\epsilon, \Gamma)\,{\rm cm^2\,erg^{-1}}. \tag{A13}$$

The function $G$ is beyond the scope of this derivation but accounts for KN effects and is described in Schlickeiser (2009). The parameter $\Gamma = \frac{4\epsilon\gamma}{mc^2}$. Plugging in equation (A13) and making the substitution $q = \frac{\epsilon}{\Gamma(\gamma mc^2 - \epsilon_\gamma}$, we are able to turn equation (A12) into

$$P_{\rm ssc}(\epsilon_\gamma, \gamma) = \frac{3c\sigma_{\rm T}}{4\gamma^2} \int_0^\infty {\rm d}\epsilon \frac{n_{\rm s}(\epsilon, t)}{\epsilon} \int_0^\infty {\rm d}\epsilon_\gamma\, \epsilon_\gamma G(q, \Gamma)\,{\rm erg\,s^{-1}}. \tag{A14}$$

Here we are going to focus on the sub-KN regime ($\Gamma < 1$ where SSC has the strongest cooling and assume that $\Gamma > 1$ has a negligible effect). More precisely, $G(q, \Gamma > 1) = 0$. This also puts a limit on $\epsilon \leq \frac{mc^2}{4\gamma}$. $\epsilon_\gamma$ is limited by the amount of energy it gain in a head-on collision $\epsilon_\gamma \leq \frac{\Gamma\gamma mc^2}{\Gamma+1}$. Applying this and changing integration variable to $q$ we get

$$P_{\rm ssc}(\gamma, t) = 12\sigma_{\rm T} c\gamma^2 \int_0^{\frac{mc^2}{4\gamma}} {\rm d}\epsilon\, \epsilon n_{\rm s}(\epsilon, t) \int_0^1 {\rm d}q \frac{qG(q, \Gamma)}{(1+\Gamma q)^3}\,{\rm erg\,s^{-1}}. \tag{A15}$$

Here the rightmost integral can be approximated as

$$\int_0^1 {\rm d}q \frac{qG(q, \Gamma)}{(1+\Gamma q)^3} \simeq \frac{1}{9} \quad \text{for} \quad \Gamma \ll 1. \tag{A16}$$

Combining this result with equation (A15),

$$P_{\rm ssc}(\gamma, t) = \frac{4}{3}\sigma_{\rm T} c\gamma^2 \int_0^{\frac{mc^2}{4\gamma}} {\rm d}\epsilon\, \epsilon n_{\rm s}(\epsilon, t)\,{\rm erg\,s^{-1}}. \tag{A17}$$

The synchrotron photon density spectrum is given by

$$n_{\rm s}(\epsilon, t) = \frac{4\pi R_{\rm em}}{c\epsilon} j_{\rm s}(\epsilon, t)\,{\rm cm^{-3}\,erg^{-1}}, \tag{A18}$$

where $R_{\rm em}$ is the size of the emission region and $j_{\rm s}(\epsilon, t)$ is given by

$$j_{\rm s}(\epsilon, t) = \frac{1}{4\pi} \int_0^\infty {\rm d}\gamma\, n(\gamma, t) p_{\rm rs}(\gamma, t)\,{\rm cm^{-3}}. \tag{A19}$$

Combining equation (A18) with equation (A19) we get

$$n_{\rm s} = \frac{R_{\rm em}}{c\epsilon} \int_0^\infty {\rm d}\gamma\, n(\gamma, t) \frac{q_0\epsilon}{2h^2\gamma^2} \pi\,{\rm CS}(x)\,{\rm cm^{-3}\,erg^{-1}}, \tag{A20}$$

where $x = \frac{2\epsilon}{3\epsilon_0\gamma^2}$. Combining equation (A20) with equation (A17), and changing the integration variable to $x$ we obtain

$$P_{\rm ssc} = \frac{3\pi\sigma_{\rm T} c\gamma^2 q_0 R_{\rm em}\epsilon_0^2}{2h^2 c} \int_0^\infty {\rm d}\gamma\, \gamma^2 n(\gamma, t) \times \int_0^{\frac{mc^2}{6\gamma^3\epsilon_0}} {\rm d}x\, x\,{\rm CS}(x)\,{\rm erg\,s^{-1}}. \tag{A21}$$

To find a nice analytic solution we limit ourselves to regime where CS($x$) is dominant. This happens when $\gamma \leq \sqrt{\frac{mc^2}{6\epsilon}}$. So here we assume CS($x$) = 0 for $\gamma > \gamma_{\rm KN} = \sqrt{\frac{mc^2}{6\epsilon_0\gamma}}$. With these assumptions equation (A21) becomes

$$P_{\rm ssc} = \frac{3\pi\sigma_{\rm T} c\gamma^2 q_0 R_{\rm em}\epsilon_0^2}{2h^2 c} \int_0^\infty {\rm d}\gamma\, \gamma^2 n(\gamma, t) \times \int_0^{\frac{\gamma_{\rm KN}}{\gamma}} {\rm d}x\, x\,{\rm CS}(x)\,{\rm erg\,s^{-1}}. \tag{A22}$$

Equation (A22) can equivalently be described by

$$P_{\rm ssc} = \frac{3\pi\sigma_{\rm T} c\gamma^2 q_0 R_{\rm em}\epsilon_0^2}{2h^2 c}\int_0^{\gamma_{\rm KN}} {\rm d}\gamma\ \gamma^2 n(\gamma,t) \times \int_0^{\infty} {\rm d}x\ x\ {\rm CS}(x)\,{\rm erg\,s^{-1}}, \tag{A23}$$

where the $x$-dependent integral is now given by Schlickeiser (2009, equation 16),

$$c_1 = \int_0^{\infty} {\rm d}x\ x\ {\rm CS}(x) = \frac{32}{81}\sqrt{3}. \tag{A24}$$

Finally, if we limit distribution to $\gamma < \gamma_{\rm KN} \simeq 1.94\times10^4 B^{=1/3}$, we can extend the limit to infinity. Resulting in

$$P_{\rm ssc} = \frac{3\pi\sigma_{\rm T} c\gamma^2 q_0 R_{\rm em}\epsilon_0^2 c_1}{2h^2 c}\int_0^{\infty} {\rm d}\gamma\ \gamma^2 n(\gamma,t)\,{\rm erg\,s^{-1}}, \tag{A25}$$

noting that

$$\int_0^{\infty} {\rm d}\gamma\ \gamma^2 n(\gamma,t) = \left\langle\gamma^2(t)\right\rangle n_0, \tag{A26}$$

we get our final expression

$$\dot{\gamma}_{\rm ssc} = \frac{3\pi\sigma_{\rm T} c q_0 R_{\rm em}\epsilon_0^2 c_1 n_0\gamma^2\left\langle\gamma^2(t)\right\rangle}{2h^2 cmc^2}\,{\rm s^{-1}}. \tag{A27}$$

To simplify remember that $q_0 = \frac{4\pi e^2}{\sqrt{3}c}$, $\epsilon = \frac{eBh}{2\pi mc}$, and $u_{\rm B} = \frac{B^2}{8\pi}$. Defining $P_0 = \frac{e^2}{\hbar^2 c2\sqrt{3}}$ and $A_0$ as

$$A_0 = \frac{3c_1\sigma_{\rm T} P_0\hbar^2 e^2 8\pi}{m^3 c^4}, \tag{A28}$$

we can find $\dot{\gamma}_{\rm ssc}$ to be equation (A29),

$$\dot{\gamma}_{\rm ssc} = A_0 R_{\rm em} n_0 u_{\rm B}\gamma^2\left\langle\gamma^2(t)\right\rangle\,{\rm s^{-1}}. \tag{A29}$$

## APPENDIX B: LSP SEDS

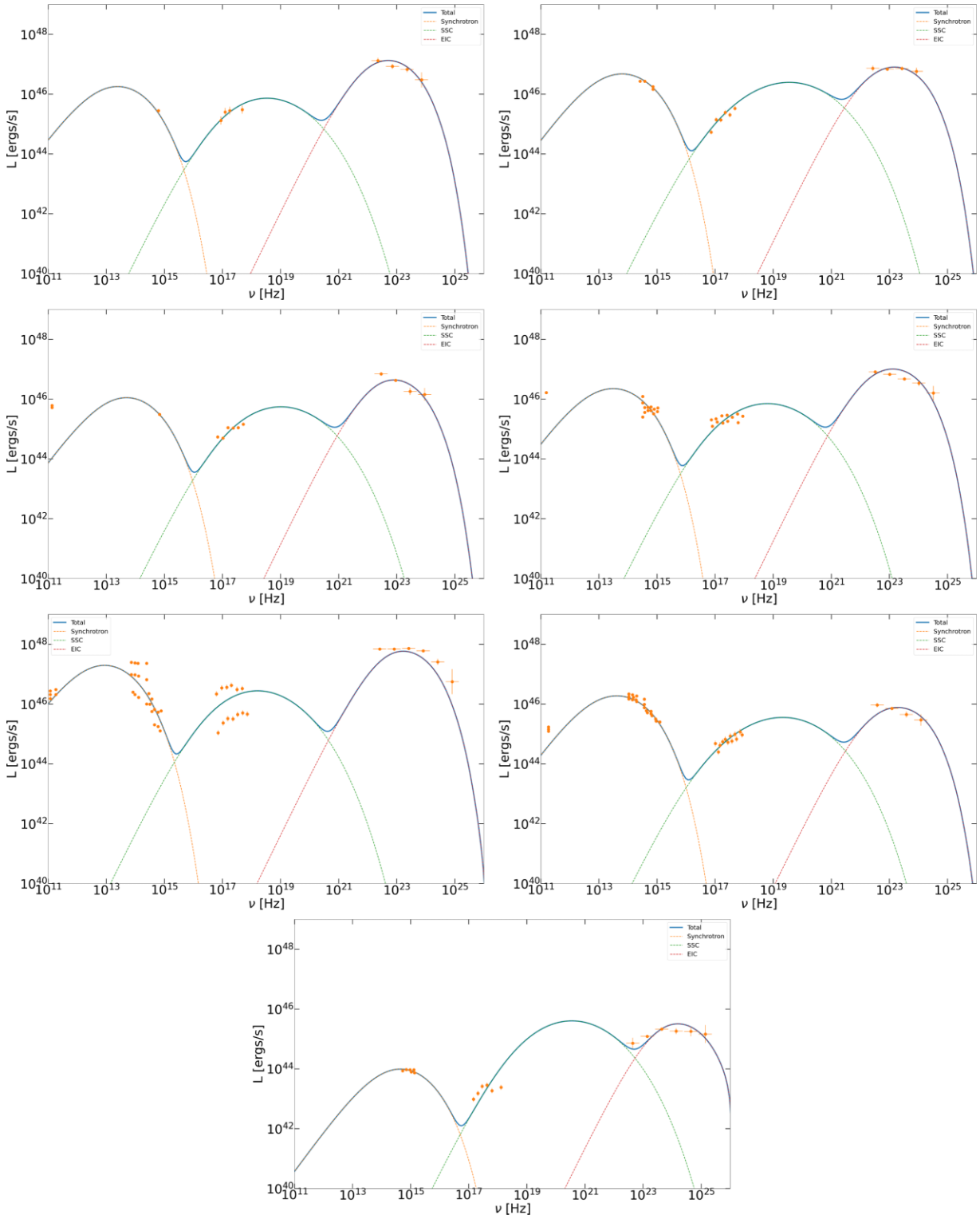


**Figure B1.** Resultant best-fitting LSP SEDs. From left to right the sources are: J0238.4+2855, J0137.1+4751, J1159.2+2912, J1256.1−0547, J0238.6+1636, J0855.4+2009, and J1719.3+1746. Solid blue line is the total emission. The dashed orange, green, and red lines are the synchrotron, SSC, and EIC components of emission, respectively.

## APPENDIX C: HSP SEDS

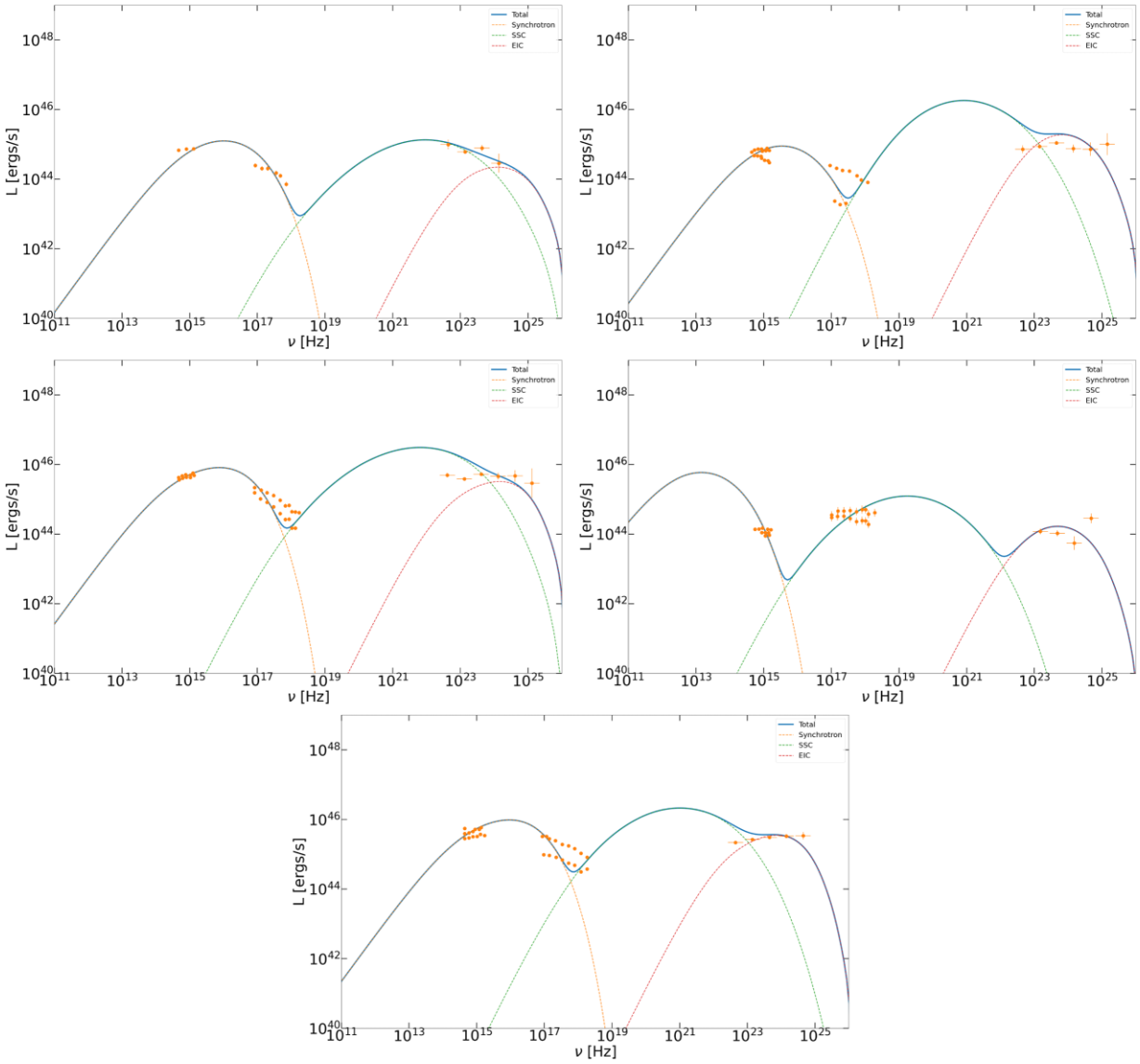


**Figure C1.** Resultant best-fitting HSP and ISP SEDs. From left to right the sources are: J1058.9+5629, J1221.7+2814, J0449.7−4348, J2000.2+6506, and J2158.8−3014. Solid blue line is the total emission. The dashed orange, green, and red lines are the synchrotron, SSC, and EIC components of emission, respectively.

This paper has been typeset from a TEX/LATEX file prepared by the author.